ASME Journal of Solar Energy Engineering
Online journal at:
https://asmedigitalcollection.asme.org/solarenergyengineering

Estefanía Vega Puga[2]
German Aerospace Center (DLR),
Institute of Future Fuels,
RWTH Aachen,
Chair for Solar Fuel Production,
Cologne 51147, Germany
e-mail: estefania.vegapuga@dlr.de

Stefan Brendelberger
German Aerospace Center (DLR),
Institute of Future Fuels,
Cologne 51147, Germany
e-mail: stefan.brendelberger@dlr.de

Anika Weber
German Aerospace Center (DLR),
Institute of Future Fuels,
RWTH Aachen,
Chair for Solar Fuel Production,
Jülich 52428, Germany
e-mail: anika.weber@dlr.de

Christian Sattler
German Aerospace Center (DLR),
Institute of Future Fuels,
RWTH Aachen,
Chair for Solar Fuel Production,
Cologne 51147, Germany
e-mail: christian.sattler@dlr.de

Modeling Development of a Receiver–Reactor of Type R2Mx for Thermochemical Water Splitting[1]

This work reports on the development of a transient heat transfer model for a prototype reactor of type R2Mx for thermochemical water splitting by temperature and pressure swing of ceria. Key aspects of the R2Mx concept, which are also incorporated in the prototype design, include a movable monolithic redox structure combined with a linear transport system, a reduction reactor, as well as a dedicated oxidation reactor. With the model, the operation of the prototype is simulated for consecutive water splitting cycles, in which ceria is reduced in a continuously heated reactor, oxidized in a separate oxidation reactor, and transported in between the reaction zones. A 2D axisymmetric numerical model of the prototype reactor was developed in ANSYS MECHANICAL. *The model includes heat transfer calculations in combination with an approximated simulation of the transport of the redox material during cyclic operation. It incorporates the chemical reaction by means of a modified heat capacity for ceria and accounts for internal radiation heat transfer inside the porous redox material by applying effective heat transfer properties. A parametric analysis has been undertaken to evaluate different modes of operation of the oxidation reactor. Model results are used to size the power demand of the reduction reactor and vacuum pump, to define durations of the process steps, as well as to assess operational parameters with respect to achieved temperatures. Findings suggest that suitable operation of the prototype reactor involves reduction durations ranging from 8 to 10 min and oxidations of 6 to 10 min.* [DOI: 10.1115/1.4065975]

Keywords: hydrogen, simulation, solar reactor

1 Introduction

Solar fuels such as hydrogen, syngas, and drop-in fuels offer a sustainable alternative to fossil fuels, and if integrated on a large scale, they have the potential to achieve an in-depth decarbonization of the industry, transport, and energy sectors. For instance, solar fuels can be used for the storage of intermittent renewable electricity, the production of process heat, as well as for long-distance transportation. To produce these renewable energy carriers, several solar approaches such as electrochemical, photochemical, and thermochemical have advanced in recent years. Of these, solar thermochemical processes have a high theoretical efficiency potential and avoid intermediate electricity generation, making them promising paths for large-scale, cost-effective solar fuel production [1]. Of particular interest are two-step thermochemical cycles based on metal oxide redox-pair systems, which are able to produce hydrogen, carbon monoxide, or syngas.

In a two-step thermochemical cycle, during the first endothermic higher temperature reduction step, the metal oxide releases oxygen and is transformed to a lower valence state under the supply of concentrated solar heat (Eq. (1)). In this study, we focus on ceria as a metal oxide, which is, thanks to its fast kinetics and long cyclic stability, regarded as one of the most attractive redox materials [2]. Ceria exhibits a nonstoichiometric behavior, in which oxygen vacancies are formed during reduction and filled during oxidation, while the lattice structure remains stable over a large range of states [3,4]. The deviation from stoichiometry, δ, is defined as a unitless oxygen vacancy concentration and depends on temperature and oxygen partial pressure. Higher reduction temperature and lower oxygen partial pressure lead to a larger δ_{red} and consequently to a higher specific fuel output.

$$CeO_{2-\delta_{ox}} \rightarrow CeO_{2-\delta_{red}} + \frac{\delta_{red} - \delta_{ox}}{2} O_2 \quad (1)$$

In the second exothermic step, namely, the oxidation, the reduced ceria is used to split H_2O (Eq. (2)) or CO_2 (Eq. (3)), or a combination of both. At the end of this step, ceria returns to its original state δ_{ox} and $\Delta\delta = \delta_{red} - \delta_{ox}$ of fuel is produced. The ceria can be used once again in the prior reduction step, thus establishing a cycle. Typical operating conditions for the reduction step are

[1]Paper presented at the proceedings of the 2023 ASME Energy Sustainability Conference, WA D.C.
[2]Corresponding author.
Contributed by the Solar Energy Division of ASME for publication in the JOURNAL OF SOLAR ENERGY ENGINEERING: INCLUDING WIND ENERGY AND BUILDING ENERGY CONSERVATION. Manuscript received October 4, 2023; final manuscript received July 8, 2024; published online August 5, 2024. Assoc. Editor: Nesrin Ozalp.

$T_{red} = 1500$ °C and $p_{O2} = 1$ mbar (Eq. (1)) and that for the oxidation step are $T_{ox} = 800$ °C and $p_{total} = 1$ bar (Eqs. (2) and (3)).

$$CeO_{2-\delta_{red}} + \Delta\delta H_2O \rightarrow CeO_{2-\delta_{ox}} + \Delta\delta H_2 \quad (2)$$

$$CeO_{2-\delta_{red}} + \Delta\delta CO_2 \rightarrow CeO_{2-\delta_{ox}} + \Delta\delta CO \quad (3)$$

To perform two-step thermochemical cycles, a number of reactors have been proposed. A wide variety of approaches including direct [5–9] or indirect [10,11] radiation of moving [6,7,12–16] or stationary particles or structures may be identified. Particle-based reactor concepts generally incorporate continuous redox material feeding and heat recuperation [6,11,17]. An important measure to benchmark the different reactor designs and process parameters is the solar-to-fuel efficiency (Eq. (4)), which is defined as the ratio of the calorific value of the amount, n_{fuel}, of fuel produced and the solar radiative energy input plus additional parasitic energy consumption of auxiliary processes such as vacuum pumping and sweep gas recycling [18].

$$\eta_{sf} = \frac{HHV_{fuel}\int_0^{t_{cycle}} \dot{n}_{fuel}(t)\,dt}{\int_0^{t_{cycle}} \dot{Q}(t) + \dot{Q}_{aux}(t)\,dt} \quad (4)$$

Particle-based reactors possess the highest theoretical efficiencies at approximately 30% [6,11]. However, the technical realization of such concepts is difficult due to challenges associated with hot (1500 °C) particle transport in combination with atmosphere control. Directly irradiated structured reactors, on the other hand, can either compose of moving or stationary structures (monoliths). Moving structures permit heat recuperation and continuous operation [13,14,19,20], while stationary structures restrict the reactor to batch mode operation and theoretical heat recovery by use of a heat transfer medium [5,21–25].

Currently, the state-of-the-art system is the cavity receiver–reactor developed under the sun-to-liquid project [5,21,22,26], which holds the highest demonstrated solar-to-fuel efficiency of 4.1% for syngas production at a 50 $kW_{thermal}$ scale in field [21]. The cavity receiver–reactor utilizes ceria reticulated porous ceramic (RPC) with dual-scale interconnected porosity (millimeter- and micrometer-sized pores within the struts) as redox material, and operates in a batch mode. During the reduction reaction, the cavity receiver–reactor is heated by concentrated solar radiation, while during the oxidation reaction, irradiation is stopped and the receiver–reactor is allowed to cool down. For this reactor, no heat recovery system is implemented, but studies have investigated its effect on the reactor system. Brendelberger et al. [24] showed that the required solar energy input for a 300 kW solar reactor could be decreased up to 40% by the integration of heat recuperation. The numerical model considered a cavity receiver–reactor coupled to a thermal energy storage (TES) utilizing purified nitrogen as a heat transfer medium. Another work [25] investigated the use of a dual storage system based on two TES and predicted a 51% increase in the solar-to-fuel efficiency considering a TES with a moderate 75% efficiency. Nevertheless, the experimental demonstration of the heat recovery system was difficult, and no actual heat recovery was achieved due to technical challenges associated with high-temperature valves (tradeoff between pressure drop and heat losses) and large heat losses throughout the piping system.

In general, one important factor for the low value obtained for the solar-to-fuel efficiency in existing reactors – compared to the theoretical efficiency potential – is the sensible heat of the RPC rejected during the temperature swing cycling. Findings suggest that achieving high solid heat recovery rates is of primary importance to reach competitive process efficiencies for this technology [25,27]. Other key features that enable a high-efficiency potential include continuous on-sun operation of the reduction reaction, favorable scale-up potential, as well as spatial separation of pressure, temperature, and reaction products [6,11,28].

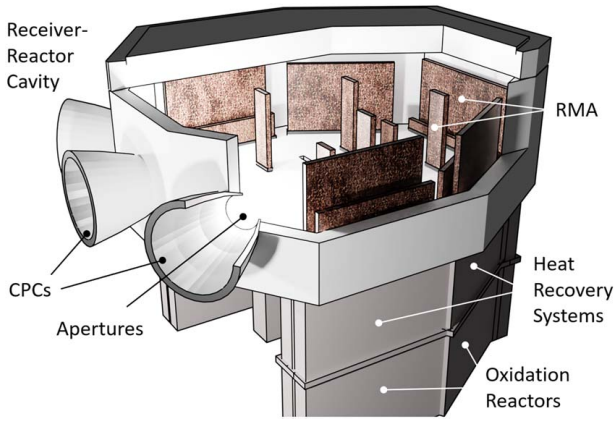

Fig. 1 MW scale vision of an R2Mx reactor design. Reproduced from Bredelberger et al. [12].

Brendelberger et al. [12] developed and presented a new moving receiver–reactor concept, R2Mx, with the aim of increasing the solar-to-fuel efficiency. The concept comprises movable monolithic redox structures, which are linearly transported between a main reduction reactor and dedicated oxidation reactors (Fig. 1). The new receiver–reactor reduces technical challenges associated with particle-based or rotating concepts by keeping the transportation system simple, while still benefiting from the high-efficiency potential of incorporating two physically distinct reaction zones. In contrast to the state-of-the-art receiver–reactor, the new concept can be operated under continuous sun irradiation, which leads to an increased efficiency of the solar interface and permits options for solid heat recovery. The initial numerical assessment of the concept predicts solar-to-fuel efficiencies above 14%, even for geometrically and operationally nonoptimized designs [12].

To date, similar moving brick reactor concepts that include solid heat recovery present no technical realization [15,29,30]. While systems including highly integrated counter-rotating rings either had parts of the system fail before reaching steady-state conditions in experimental campaigns [13,14] or no experimental data are available [20]. As such, the experimental development and demonstration of the R2Mx receiver–reactor is not only critical to the technology's advancement but also to prove the technical feasibility of solid heat recovery. A step-wise approach is applied for the development of the R2Mx technology. Within a prototype test stand, a set of key innovations for the technology and their integration are being pursued, while other aspects of the technology will be developed and integrated at a later stage. Before the proof-of-concept test stand aiming at the experimental demonstration of the key features of the R2Mx design can be built, an in-depth analysis of the system behavior is necessary.

In this work, we present the development of a 2D transient heat transfer model of the R2Mx prototype test stand design, based on the initial 1D model presented in the work of Brendelberger et al. [12]. The numerical model is aimed at supporting the design development by providing an in-depth understanding of the underlying heat transfer and the evolution of the temperature distribution within the prototype test stand. The focus of this study lies in the development of the test stand components and the demonstration of the technical feasibility of the R2Mx concept. Notable differences between the proposed R2Mx scaled-up vision (Fig. 1) and the protype test stand are the use of only one redox material assembly (RMA), the use of electric heating instead of heating by concentrated solar radiation, missing solid heat recovery, and the shape of the RMAs. The modular approach of the concept allows addressing these aspects in subsequent studies. With such a system, the direct comparison of the prototype test stand to solar receiver–reactors is limited due to its electric heating approach, as discussed in Sec. 2. In order to prevent confusion with solar-to-fuel efficiencies, a different

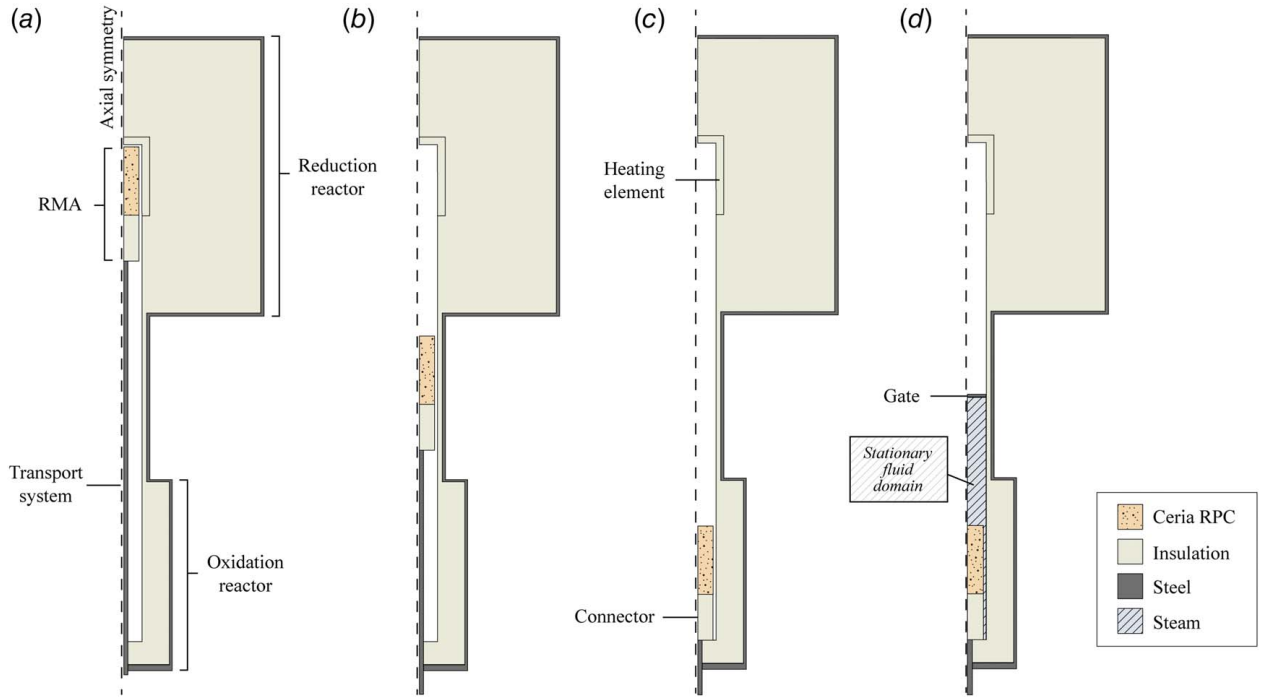

Fig. 2 Prototype test stand design. (*a*) RMA in the reduction reactor, (*b*) RMA on its way from the reduction reactor to the oxidation reactor, (*c*) RMA being placed in the oxidation reactor, and (*d*) RMA undergoing oxidation with oxidation reactor closed. The transport system has been cropped vertically in (*b*)–(*d*) for illustration purposes. Diagonal hatching shows the stationary fluid domain, and all other components are modeled in the solid domain.

metric, the energy conversion ratio (Eq. (17)), is used to analyze the system.

With the numerical model, we examined temperature profiles within each component to evaluate the initial material selection and to give recommendations. Components, namely, the heating unit and vacuum pump, are sized, and a parametric analysis to investigate different modes of operation of the oxidation reactor is undertaken. Durations of the process steps to ensure reasonable operation of the prototype test stand are also estimated.

2 Prototype Test Stand Configuration

The initial prototype test stand comprises an RMA, a reduction reactor, a transport system, and an oxidation reactor; its configuration is shown schematically in Fig. 2. This test stand shows some of the unique features of the R2Mx receiver–reactor, namely, two physically distinct reaction zones (reduction and oxidation reactors), linear transportation of the reactive ceria RPC, and atmosphere control between reaction zones. However, unlike the scaled-up vision of the R2Mx concept (Fig. 1), the prototype test stand has electric heating instead of a solar interface, no heat recovery system, and cylindrical reactive monoliths instead of planar ones.

The primary aim of the prototype test stand is to prove the technical feasibility of innovative key components of the R2Mx concept by their development and the demonstration of their sustainable operation for a prolonged period of time. Therefore, in this initial development stage, instead of using solar radiation in a receiver–reactor to heat the ceria RPC, a resistive heating element surrounding the RPC in the reduction reactor is chosen for simplicity. The heating element serves as heat source in the proof-of-concept test stand. The use of cylindrical ceria RPCs, instead of planar ones, allows the utilization of commercially available off-the-shelf vacuum components in the prototype test stand. This leads to a more rapid development of reactor components relevant to the R2Mx concept.

Considering the aforementioned characteristics of the prototype test stand, it is awareness of the authors that the operation of the test stand prototype will differ from the operation of the scale-up vision. For instance, the heating of the redox material and resulting temperature gradients will be different due to the dissimilar RPC geometry and related radiation heat transfer properties within the bulk and at the surface of the redox material. Similarly, the redox material heating with concentrated solar radiation will differ from the currently modeled electrical heating in terms of heating rate, especially if the ceria RPC is directly irradiated. The exchange of the redox material's geometry and heating source will be addressed at later stages of the development.

In the prototype test stand, the RMA includes a ceria RPC and an Al_2O_3-SiO_2 insulation segment that serves as a connector to the transport system. Both the ceria RPC and the connector have a cylindrical shape with an outer diameter of 70 mm. The redox material has a height of 150 mm, while the connector has a length of 100 mm. The ceria loading corresponds to approximately 1 kg. In the prototype design, only one RMA is included, but in later development stages, the use of more RMAs is fundamental to achieve continuous on-sun operation of the R2Mx reactor.

In the model of the prototype design, the reduction reactor has been simplified, and many components have been kept generic at this development stage. For example, the transport system is represented simplified by a 20 mm diameter stainless steel (316L) rod, which moves the RMA between the two reaction zones, without representing the motor unit. Moreover, the oxidation reactor is represented by a 420 mm high chamber comprising a 60 mm thick Al_2O_3-SiO_2 (Altraform KVR 164-502) insulation [31] and a 5 mm stainless steel shell. This reactor also possesses inlets to inject steam, outlets to extract the product gas, and a connection to the vacuum pump to evacuate the reactor. Pressure sealing between the reaction zones is indicated by a 5 mm thick stainless steel gate, which is closed during oxidation while steam is injected during oxidation (Fig. 2(*d*)).

3 Heat Transfer Analysis

The prototype test stand design, which features axial symmetry, was simulated using a two-dimensional axisymmetric heat transfer model implemented in the commercial software ANSYS MECHANICAL. The simulation procedure represents the sequential execution steps

under consideration of the operating conditions. Details on the simulation procedure are given below.

3.1 Simulation Workflow. Initially, a first reduction of the RMA is simulated followed by sequential simulations, which illustrate the operational steps: RMA transport to the oxidation reactor, cooling, oxidation, RMA transport to the reduction reactor, and once more (a new) reduction. These operational steps are simulated consecutively (in the order previously stated) to accurately reflect the foreseen operation of the prototype test stand and to investigate the interactions and dependencies between the different stages of the thermochemical water splitting cycle in our setup. A complete cycle comprises one oxidation and one reduction, as well as the intermediate cooling and transport steps. The simulation was conducted for five cycles in the base case and for three cycles during the parametric analysis. The simulated operation of the prototype test stand is based on the literature data (reduction temperature, start of oxidation temperature, and specific oxidant flowrate) from previously undertaken experimental campaigns of the state-of-the-art cavity receiver–reactor [21,32].

For the first reduction, the RMA is placed in the reduction reactor while the heating element is kept at 1500 °C. To derive realistic starting conditions for the cycle, a steady-state solution is calculated. During the time at which the reactor prototype is under vacuum (reduction, RMA transport, and cooling), the gas atmosphere in the setup is neglected. This is justified since previous studies have demonstrated that the contribution of convective heat transfer is negligible when operating under similar vacuum conditions [22,33].

Next, to simulate the transport of the RMA into the oxidation reactor, the complete movement trajectory is discretized into several separate steps and RMA positions. To solve the governing equation at each intermediary RMA position, the resulting temperature distribution obtained from the previous position was imported as the initial condition. Then, a transient thermal simulation considering radiation, conduction between components, and ambient losses is run. The entire RMA movement from reduction to oxidation chamber was assumed with a duration of 4 s, which determines the duration of the single-step simulations accordingly. When comparing the effect of the RMA trajectory discretization count, already when going from two to three positions, the ceria RPC shows only a 0.22% enthalpy change due to the short transport step duration. Considering this reduced effect and in order to limit the computational effort, it was decided to represent the transport step by only two positions (Figs. 2(*b*) and 2(*c*)).

Once the redox material reaches the oxidation reactor, the ceria RPC is allowed to cool down. The objective of the cooling step is to reach a target RPC mean temperature of approximately 900 °C in the first cycle. In light of this, a cooling step duration of 5.5 min is determined. This cooling step duration remains constant throughout all the cycles.

After the redox material's cooling step has finalized, steam is injected and the oxidation reaction starts. During the oxidation, the oxidation reactor is operated in a steam atmosphere at 1 bar, which is modeled by the introduction of a fluid phase in the oxidation reactor (Fig. 2(*d*)). The injected steam and the gate have an initial temperature of 150 °C, while for the rest of components, the initial temperature distribution is the solution from the previous simulation. The steam has a temperature of 150 °C to reduce condensation inside the oxidation reactor. Nevertheless, during the prototype test stand operation, it is recommended to pressurize the oxidation reactor with an inert gas, as described in the literature [21,32], to avoid condensation occurring as a result of lower pressures in the reactor. The oxidizer flow rate is 0.0135 l/s and was estimated using data from experimental campaigns of the cavity receiver–reactor reported in the literature [22] and the ceria mass in the prototype design. In total, the oxidation has a duration of 8 min in the base case, and throughout this time, the reduction reactor is continuously heated.

During the oxidation reaction, the gate is closed, disconnecting the atmospheres of the two reactors. In the simulation, this is represented by the introduction of a steel plate in between the reactors. Additionally, during oxidation, the reduction reactor is continuously heated by means of the heating element. The oxidation step is simulated by using a series of transient simulations coupled to each other, in which the solution from the previous simulation is used as the initial condition for the next. At the modeling stage, the design of the inlet and outlet as well as the resulting flow pattern inside the oxidation reactor had not been decided upon. In this first simplified numerical design study, no actual computational fluid dynamics (CFD) calculation was implemented, instead the fluid (steam) was modeled as stationary. The effect of the exchange of the oxidant fluid on the system is approximated by a complete replacement of the fluid with a cold steam for each step in the simulation series. The volumetric flowrate of the oxidant gas, the free volume in the oxidation reactor, and the duration of the oxidation step affect how frequently the steam volume is exchanged. For the base case, the steam volume was replaced ten times. This strong simplification captures to some extent the enthalpy of the fluid streams entering and leaving the oxidation reactor, but disregards flow patterns, the effect of the inlet and outlet geometry, as well as natural or forced convection. At a later stage in the development process, this assumption will be replaced by CFD simulations.

Immediately upon the end of the oxidation step, the separating steel plate and fluid component are removed, and the RMA is transported to the reduction reactor, performing a new cycle. The procedure to simulate the RMA movement is as previously described during its way to the oxidation reactor. The reduction steps, excluding the first one, do not have a fixed time duration, but are controlled by a new metric, the energy conversion ratio (Eq. (17)). This new metric, which is presented in the following section, is introduced to assess the design and operational choices of the reactor system.

During the reduction, RMA transport, and cooling steps, the gas atmosphere in the setup is neglected for the heat transfer simulation, given that operation under 1 mbar vacuum is considered. All the reactor components, including the porous ceria RPC, are modeled as solid domain. During oxidation, the steam is modeled as a stationary fluid domain.

3.2 Governing Equations and Boundary Conditions. The transient energy conservation (Eq. (5)) is discretized and solved by a finite element analysis (FEA) using ANSYS MECHANICAL. The conservation equation in the solid domain is given by

$$\nabla\,(k\,\nabla T) + \boldsymbol{q}_{\text{conv}} + \boldsymbol{q}_{\text{rad\_sur}} + \boldsymbol{q}_{\text{rad\_amb}} = \rho c_{\text{p}} \frac{\partial T}{\partial t} \tag{5}$$

where k is the thermal conductivity, ρ the density, c_{p} the specific heat capacity, $\boldsymbol{q}_{\text{conv}}$ the convective heat flux to ambient as the boundary condition, $\boldsymbol{q}_{\text{rad\_sur}}$ the radiative heat flux between surfaces inside the reactor, and $\boldsymbol{q}_{\text{rad\_amb}}$ the radiative heat flux to ambient as the boundary condition.

Losses to ambient were considered at the outer steel surfaces of the reactor via two heat transfer modes, namely, convection and radiation. Convection to ambient was implemented according to Eq. (6), considering a film coefficient, h, of 5 W/Km^2. Radiation to ambient used Eq. (7) with a steel emissivity, ε_s, of 0.57. In both cases, ambient temperature is set to 22 °C. Radiation between surfaces inside the reactor prototype was accounted for via Eq. (8). All reactor components except the steam participate in radiation.

$$\boldsymbol{q}_{\text{conv}} = h\,A\,(T_{\text{s}} - T_{\text{amb}}) \tag{6}$$

$$\boldsymbol{q}_{\text{rad\_amb}} = \varepsilon_{\text{s}}\,\sigma\,({T_{\text{s}}}^4 - {T_{\text{amb}}}^4) \tag{7}$$

$$\boldsymbol{q}_{\text{rad\_sur},i} = \varepsilon_i\,\sigma\,T_i^4 + \rho_i \sum_{j=1}^{N} F_{ij}\boldsymbol{q}_{\text{rad\_out},j} \tag{8}$$

Table 1 Material properties of ceria RPC

Variable	Correlation	Unit
Dual-scale porosity	$\Phi_{dual} = 0.7622$	–
Number of pores per inch	ppi = 10	ppi
Density RPC	$\rho_{RPC} = 1716.916$	kg/m^3
Emissivity [34]	$\varepsilon_{RPC} = 0.5$	–
Extinction coefficient [34]	$\beta = 390.962$	1/m
Thermal conductivity CeO_2 [22]	$k_{CeO_2} = -1.723 \times 10^{-9} \cdot T^3 + 1.12 \times 10^{-5} \cdot T^2 - 0.024 \cdot T + 17.8$	W/m K
Porous thermal conductivity [22]	$k_{por} = k_{CeO_2}(1 - 0.6223\,\Phi_{dual})(1 - 1.055\,\Phi_{dual})$	W/m K
Radiative conductivity [20]	$k_{rad} = \frac{16\,\sigma T^3}{3\,\beta}$	W/m K
Effective thermal conductivity	$k_{eff} = k_{por} + k_{rad}$	W/m K
Reduction extent [22] (T in °C)	$\delta = 10^{-(2.15\times10^{-6}T^2 - 9.88\times10^{-3}T + 12.2)} \cdot \left(\frac{p_{O_2}}{p_0}\right)^{1.25\times10^{-7}T^2 - 3.1\times10^{-4}T - 1.83\times10^{-2}}$	–
Reaction enthalpy [22]	$\Delta H_O = 484.705 - 251.870\,(\Delta\delta)^{0.5}$	kJ/mol
CeO_2 specific heat capacity [22]	$c_{p,mat} = \frac{67.95 - 9.9 \times 10^5 \cdot T^2 + 0.0125 \cdot T}{M_{CeO_2}}$	J/kg K
Heat capacity due to chemical reaction [35]	$c_{p,chem} = \frac{dQ_{red}}{d(\Delta\delta)} \cdot \frac{d(\Delta\delta)}{dT} = \Delta H_O \cdot \frac{d(\Delta\delta)}{dT}$	J/kg K
Modified effective heat capacity [35]	$c_{p,eff} = c_{p,mat} + c_{p,chem}$	J/kg K

where A is area, ε is emissivity, σ is the Stefan–Boltzmann constant, and F_{ij} is the view factor from surface i to surface j.

The energy conservation equation for porous ceria RPC, which is modeled as a solid domain, is

$$\nabla\,(k_{eff}\,\nabla T) + \boldsymbol{q}_{rad\_sur} = \rho_{RPC}\,c_{p,eff}\,\frac{\partial T}{\partial t} \tag{9}$$

where k_{eff} is the effective thermal conductivity of the RPC, ρ_{RPC} the density of the reactive material considering its porosity, and $c_{p,eff}$ the modified specific heat capacity. The heat associated with the chemical reaction is not included in a separate source term, but an implementation using a modified specific heat capacity for the ceria RPC is applied. The modified heat capacity, $c_{p,eff}$, correlates the reduction enthalpy, the change in δ, and change in energy required to heat one mole of ceria with the material-related specific heat capacity of ceria (Table 1).

For the fluid domain (steam), which is assumed to be stationary, the energy conservation is given by

$$\nabla\,(k\,\nabla T) = \rho c_p\,\frac{\partial T}{\partial t} \tag{10}$$

Perfect thermal conductance between all domains is assumed.

3.3 Thermodynamics and Metrics. The thermodynamic properties used have an analytical form, with correlations obtained from the literature [22,36]. The model was written in PYTHON 3.11 and assumes that all reactions between the redox material and the gas phase reach equilibrium, which is justified by the fast kinetics of the reduction reaction (Eq. (1)) and the length of the oxidation step. The reduction extent of ceria is modeled using the thermodynamic equilibrium correlation reported by Zoller et al. [22] (Table 1). It is the knowledge of the authors that the oxidation reaction in the examined temperature range, on the contrary to the reduction, is controlled by surface processes with apparent first-order dependence toward steam concentration [37]. However, we consider that the usage of the thermodynamic equilibrium for the purposes of estimating temperature distributions in the oxidation reactor leads to acceptable approximations, given that the integral of the enthalpy converges to a value close to the equilibrium enthalpy. Furthermore, for the water splitting reaction, the model developed by Holzemer-Zerhusen et al. [36] is utilized. The equilibrium of Eq. (11) is calculated using the law of mass action as per Eq. (12).

$$H_2O \leftrightarrow H_2 + \frac{1}{2}O_2 \tag{11}$$

$$K_{eq} = \frac{\frac{p_{H_2}}{p_0} \cdot \left(\frac{p_{O_2}}{p_0}\right)^{\frac{1}{2}}}{\frac{p_{H_2O}}{p_0}} \tag{12}$$

where p_{H_2}, p_{O_2}, and p_{H_2O} are partial pressures and p_0 is the standard pressure, 1 bar. The oxygen partial pressure in the oxidation chamber can be determined by Eq. (13), by rearranging Eq. (12) and introducing, X_{ox}, the conversion of H_2O.

$$p_{O_2,ox} = p_0\left(\frac{K_{eq}\,(1 - X_{ox})}{X_{ox}}\right)^2 \tag{13}$$

$$X_{ox} = \frac{n_{H_2}}{n_{H_2O}} = \frac{n_{H_2O,initial} - n_{H_2O,final}}{n_{H_2O,initial}} \tag{14}$$

$$n_{H_2O,final} = n_{H_2O,initial} - (\delta_{red} - \delta_{ox})n_{Ce} \tag{15}$$

The reaction constant, K_{eq}, is determined as a function of the free Gibbs energy of reaction according to Eq. (16). $\Delta_R G$ is calculated with data obtained from the software FACTSAGE 7.0 [38].

$$K_{eq} = \exp\left(-\frac{\Delta_R G}{R\,T_{ox}}\right) \tag{16}$$

The calculated oxygen partial pressure during oxidation as well as the redox material's oxidation temperature is used to estimate the reduction extent at the end of oxidation and therefore also the fuel yield per cycle.

A new metric is introduced to assess the design and operational choices analysis: the energy conversion ratio (Eq. (17)).

$$r_{econv} = \frac{n_{H_2} HHV_{H_2}}{Q_{Heating\ element}} \tag{17}$$

where n_{H_2} refers to the amount of hydrogen produced in one cycle and $Q_{\text{Heating element}}$ is the energy demand required to maintain the heating element at a constant temperature (1500 °C). The energy conversion ratio is used to determine a reasonable duration of the reduction steps (from second reduction onward) and is also evaluated at the end of each cycle. Once the maximum energy conversion ratio is achieved, the reduction step is stopped, thus avoiding energy-intensive long-term heating, which only results in negligible reduction extent gains. The pressure during the reduction is assumed constant at 1 mbar (0.1 mbar and 10 mbar during the parameter study).

The energy conversion ratio unlike the solar-to-fuel efficiency (Eq. (4)) does not account for energy losses associated with auxiliary processes such as operating a vacuum pump or evaporating water, meaning that the energy conversion ratio cannot be used for technology benchmarking. The aim of the R2Mx prototype test stand development is to demonstrate the technical feasibility of the R2Mx concept by developing reactor components, and therefore, efficiency optimization is out of the scope of this study. Additionally, unlike the other receiver–reactors developed for thermochemical water splitting, this first prototype does not count with a solar interface, and therefore, the derivation of a solar-to-fuel efficiency would result in a rather large uncertainty.

3.4 Material Properties. Material properties of the ceria RPC are listed in Table 1. All reactor components are simulated like solid domains, including the porous ceria RPC, which is modeled using effective material properties. Radiative heat exchange within the RPC is described by the Rosseland diffusion approximation in the radiative conductivity part of the effective thermal conductivity k_{eff}. The Rosseland diffusion approximation is used in light of its reduced computational demand while still assuring reasonable accuracy (~2% error) when estimating the temperature of ceria RPC structures, as reported in the literature [20]. Direct penetration of radiation into the depth of the material is not considered. Furthermore, properties of the insulation, steel, and steam are given in Table 2. They were extracted from literature and from the ANSYS database.

3.5 Discretization and Numerical Error. To discretize the governing equation in space, approximately 24,700 quadrilateral elements were used. Inflation layers were included on the ceria RPC's surface, insulation connector's surface, as well as on the surface of the insulation from the oxidation reactor. Largest mesh elements have a square geometry with an edge length of 2.5 mm and are located in the inner area of the reactor components. However, smallest elements have a thickness of about 0.07 mm and 2.5 mm height and are located within the inflation layers. The axisymmetric mesh was realized in 2D and solved using radial symmetry. A mesh independence study considering three meshes at different coarseness (~12,500, 25,000, and 50,000 elements per mesh) was completed. The selected mesh resulted in approximately a 0.2% difference at monitored points of the different components compared to the finest mesh, while significantly reducing computational times. For the discretization of time during RMA transport, a constant step size of 0.02 s was used. During the reduction and oxidation steps, the program-controlled time-stepping option was selected for automatic time-step optimization.

The numerical error associated with the simulation method is estimated to be about 5.5%, as reported in literature for a very similar investigation utilizing the same software [43]. This error refers to an imbalance in the heat equation, which is linked to the time and space discretization of the model in ANSYS MECHANICAL. Additionally, a minimal difference (0.01%) between the average temperature of the exported results and the average temperature of the imported data has been identified. This error could be addressed in the mapping of the imported temperature profiles on different meshes. Even though the total error is relatively high, it is considered acceptable with respect to the goals of the study.

4 Results and Discussion

The numerical model is a useful tool for the development of the reactor prototype, as it can be utilized to assess the selection of various design choices and operating conditions. In the subsequent section, a base case simulation, with key operational parameters summarized in Table 3, is first analyzed. Temperature profiles within each component are reviewed and used to evaluate the initial material selection. Next, the heating unit and vacuum pump are sized, and finally, a parametric analysis utilizing four scenarios is used to investigate different modes of operation of the oxidation reactor.

4.1 Temperature Distribution and Evolution. To provide an understanding of the expected temperature distribution of the prototype test stand design, a contour plot is displayed in Fig. 3. Figure 3(*a*) portrays the prototype at the end of the first reduction step, while Fig. 3(*b*) shows the prototype at the end of the fifth oxidation step. Throughout the entire five cycles, the heating element is uniformly maintained at 1500 °C. In general, during reduction, the

Table 2 Properties of reactor components

Variable	Correlation/value	Unit
Insulation Al_2O_3-SiO_2		
Density [31]	$\rho_{\text{ins}} = 500$	kg/m^3
Specific heat capacity [31]	$c_{\text{p,ins}} = -3.09\times10^{-10}\,T^4 + 1.71\times10^{-6}\,T^3 - 3.48\times10^{-3}\,T^2 + 3.18\,T + 101$	J/kg K
Thermal conductivity [31]	$k_{\text{ins}} = \begin{cases} 6\times10^{-11}\,T^3 - 1\times10^{-8}\,T^2 - 1\times10^{-5}\,T + 0.1802, & T < 1500\ ^\circ\text{C} \\ 0.29, & T \geq 1500\ ^\circ\text{C} \end{cases}$	W/m K
Emissivity [39]	$\varepsilon_{\text{ins}} = 0.28$	–
Stainless Steel 316L		
Density [40]	$\rho_{\text{ss}} = 7850$	kg/m^3
Specific heat capacity [40]	$c_{p,\text{ss}} = 412 + 0.2\,T - 2\times10^{-5}\,T^2$	J/kg K
Thermal conductivity [40]	$k_{\text{ss}} = 0.013\,T + 11.45$	W/m K
Emissivity [41]	$\varepsilon_{\text{ss}} = 0.57$	–
Steam (150 °C, 1 bar)		
Density [42]	$\rho_{\text{st}} = 0.51634$	kg/m^3
Specific heat capacity [42]	$c_{p,\text{st}} = 1985.7$	J/kg K
Thermal conductivity [42]	$k_{\text{st}} = 0.0261$	W/m K

Table 3 Operational parameters of base case simulation

Variable	Value	Unit
Heating element temperature	1500	°C
Partial pressure of oxygen in reduction reactor	1	mbar
Steam flowrate	0.0135	l/s
Cooling duration	5.5	min
Oxidation duration	8	min

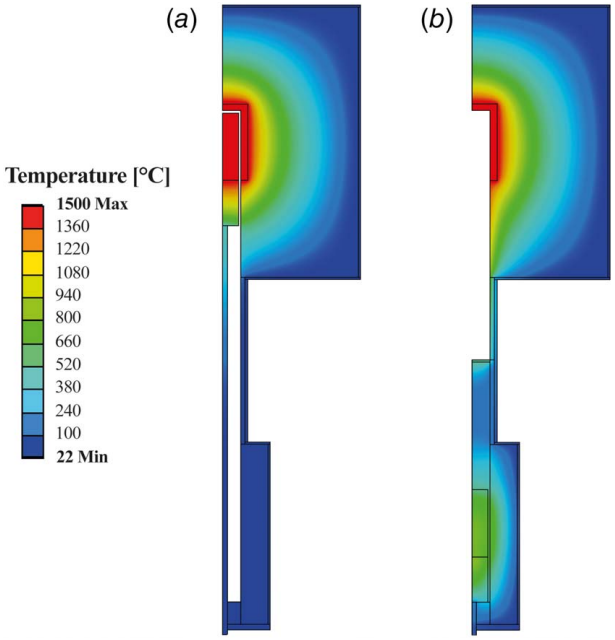

Fig. 3 Temperature distribution of the prototype test stand design components: (*a*) after first reduction step and (*b*) at the end of the fifth oxidation step. The transport system has been cropped vertically in (*b*) for illustration purposes.

RMA reaches its highest temperature, while during oxidation, the RMA reaches its minimum temperature. On the contrary, the components of the oxidation reactor are the hottest during oxidation and coldest during reduction.

At the end of the first reduction, the ceria RPC reaches an average temperature of 1489.2 °C, where the maximum temperature is 1499.7 °C, while the minimum temperature is 1447.8 °C. The redox material's average temperatures after the second, fourth, and sixth reduction steps are 1491.3 °C, 1466.6 °C, and 1464.7 °C, respectively. For a comprehensive understanding of the ceria RPC temperature distribution, the reader is referred to Figs. 4(*a*) and 4(*b*), where details on the amount of redox material at a given temperature are shown for cycles one, three, and five. After the first oxidation, the ceria RPC reaches its lowest volume average temperature of 689.6 °C. While after the third and fifth oxidation steps, the average temperature is 747.1 °C and 761.3 °C, respectively. Findings indicate that the average temperature of the redox material after oxidation increases as the number of cycles also increases (Fig. 4(*c*)). When the average temperatures obtained at the end of the oxidation steps are extrapolated using a negative exponential fit, a rough approximation for the average temperature at larger cycles, when the temperatures of the system have stabilized, can be made (Fig. 4(*d*)). The exponential fit, which utilizes five data points, has an R^2 value of 0.999, showing a good data fit. After ten cycles, the minimum average redox material temperature converges and is estimated to be approximately 764 °C. This expected RPC's temperature after oxidation is higher than reported temperatures from experimental campaigns of the cavity receiver–reactor. Studies indicate a nominal RPC temperature after oxidation of 500 °C for a 5 kW_{th} reactor [32] and 650 °C for a 50 kW_{th} reactor [21], showing that similar operational conditions that were successful in producing solar fuels could be achieved with our setup. The herein shown increase in average temperature of the RPC with the increasing number of cycles is related to the fact that the insulation in the oxidation reactor also warms up with consecutive cycles.

During the ceria RPC transport between the reaction zones, the average temperature of the redox material decreases by only approximately 3.3 °C, which equates to about a 0.2% loss. In contrast, when considering the cooling between reduction and oxidation, the redox material's temperature decrease is on average 50%. This demonstrates that the transport step has only a minor impact on the RPC's cooling. This phenomenon can be linked to the duration of each step, seeing that transport takes only 4 s, while the complete cycle is approximately 22 min and occurs even though the RPC passes through cooler sections along its way between the reactors. The optimization of the transport step duration is constrained by mechanical integrity of the RMA if the movement is excessively rapid (4 s are considered with respect to this as a conservative transport step duration). Conversely, extending the transport step duration may be considered; however, this adjustment could lead to increased heat losses of the RPC during transport, reflecting on the need to reduce the cooling step duration.

At the end of the first reduction step, the insulation connector has a maximum temperature of 1461.7 °C at the surface where it is in contact with the ceria RPC. The connector's temperature gradually decreases in the vertical direction, reaching a minimum of 363.1 °C directly where the transport system is located. In general, during oxidation, the connector has a higher maximum temperature than the redox material due to its large specific heat capacity, $c_{p,\mathrm{ins}}$, and low conductivity, k_{ins}. After the fifth oxidation, the connector has a maximum temperature of 880.7 °C and a minimum temperature of 195 °C. Given the temperatures that the connector material is subjected to, the choice of insulation material (Al_2O_3-SiO_2) appears appropriate as it has a high classification temperature of 1600 °C.

The transport system rod reaches its maximum temperature of 491.6 °C after the sixth reduction at the surface where it is in contact with the insulation connector. If a lower maximum temperature of the transport system would be desired the length of the insulation connector could simply be increased. Nevertheless, this maximum temperature does not pose a problem for operation of stainless steel. While oxidation occurs the majority of the transport system is outside of the reactor and can cool through radiation and convection to the ambient. After the fifth oxidation, the maximum temperature of the transport rod is 198 °C, where the transport rod meets the connector. In the transport rod area that is outside the reactor, the maximum temperature is 140 °C and the minimum temperature is 90.6 °C. The transport system is mainly heated through conduction by the connector, but is also heated through radiation by the oxidation reactor's insulation when the RMA is held in the reduction reactor (position as in Fig. 2(*a*)). It is because of this radiative heat exchange with the oxidation insulation that after the fifth reduction step the transport system reaches its maximum temperature of 140 °C in the area outside the reactor.

The insulation of the reduction reactor has a maximum temperature of 1500 °C, since it is in direct contact with the heating element. Throughout the three cycles, the temperature distribution in the insulation of the reduction reactor remains fairly similar, with the temperature decreasing through the insulation's depth. The minimum temperature remains constant through the entire simulation at 37.5 °C.

The insulation of the oxidation reactor is an important component of the prototype. As the cycles progress, it warms up as shown in Fig. 5(*a*). The minimum average temperature of the oxidation reactor's insulation is 27.4 °C, when the first cycle begins. During the first cycle, the maximum average temperature is 175.6 °C, while for the third and fifth cycles, it is 238.2 °C and 260.2 °C, respectively. When the maximum average temperature of the oxidation reactor's insulation is extrapolated using a negative exponential

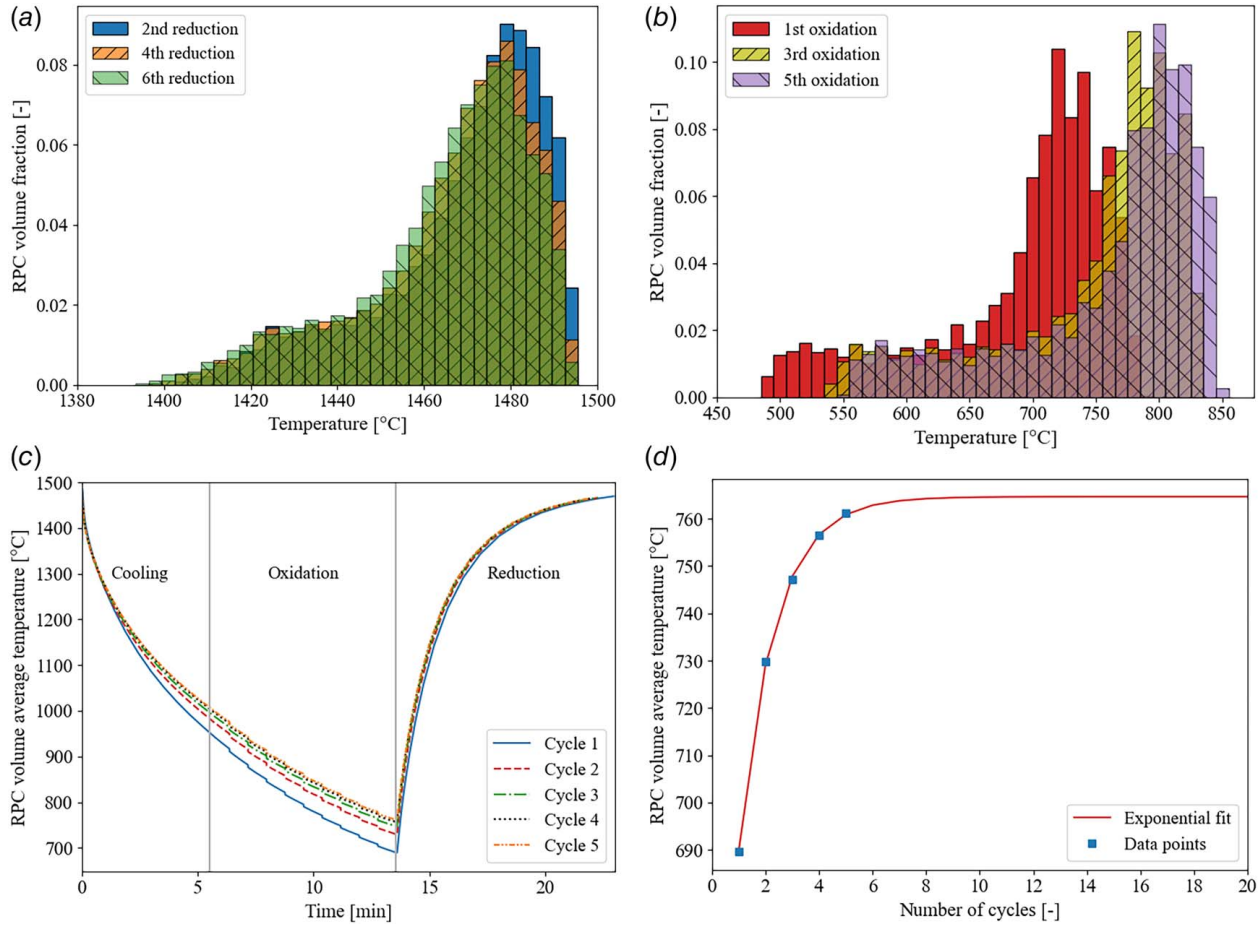

Fig. 4 (*a*) Temperature distribution of the ceria RPC at the end of the reduction steps, (*b*) temperature distribution of the ceria RPC after the oxidation steps, (*c*) volume average temperature of the ceria RPC during the entire cycle duration, and (*d*) fitting of average temperature of ceria RPC after oxidation with increasing number of cycles. Base case operational parameters are given in Table 3.

fit, the maximum average temperature increases and converges at approximately 271 °C for 15 cycles (Fig. 5(*b*)). This estimate considers a fitting based on five data points and an R^2 value of 0.984.

The maximum temperatures in the oxidation reactor's insulation occur as the hot ceria RPC is initially placed in the oxidation reactor. The maximum insulation temperature during the entire simulation arises during the fifth cycle and is 1248.1 °C. This maximum temperature only develops on a very thin section along the surface of the insulation, which only represents a minuscule percentage (0.15%) of the insulation's volume. After the oxidation

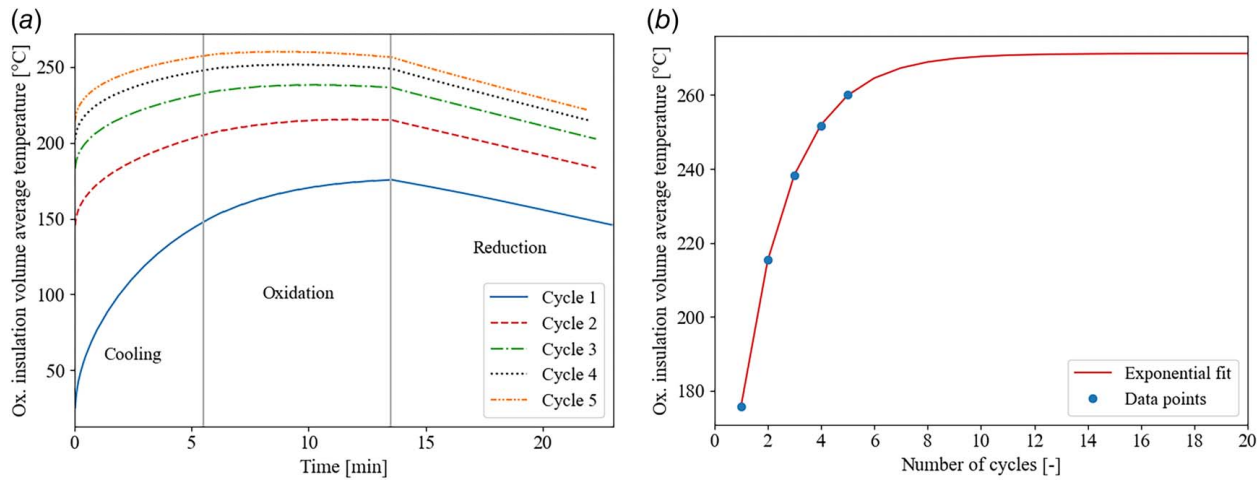

Fig. 5 (*a*) Volume average temperature of the oxidation reactor's insulation during the entire cycle and (*b*) fitting of maximum temperature of insulation after oxidation with the increasing number of cycles. Base case operational parameters are given in Table 3.

reaction is finished and the RMA is transported to the reduction reactor, the insulation of the oxidation chamber progressively cools down. On average the insulation cools down by 7.5% from the end of the oxidation reaction to the start of a new one. The minimum of the average temperature values for the first, third, and fifth cycles are 148.4 °C, 183.2 °C, and 214.6 °C, respectively.

The insulation of the oxidation reactor does not reach as high temperatures as the insulation in the reduction reactor or the connector; however, as an initial estimate, they are modeled using the same material. The usage of another more cost-effective insulation material with a lower classification temperature could be evaluated in future endeavors, considering its effect on the ceria RPC's minimum temperature and the cycle's performance. Furthermore, investigations assessing the effect of the geometry (e.g., thickness) of the oxidation reactor's insulation on overall performance of the test stand will be undertaken.

The gate that separates the reaction zones initiates every oxidation step at a temperature of 150 °C. This temperature was assumed considering the oxidant's initial temperature (also 150 °C) and heat transfer to the gate while it is open, which during this simulation is not modeled. The gate's final average temperature is approximately 400 °C. The dominant form of heat transfer to the gate is through radiation from the heating element in the reduction reactor. As the gate is anticipated to perform cyclic operations involving repeated opening and closing, the implementation of high-vacuum metallic seals is not advisable. Suitable materials for this application include high-temperature-resistant elastomers like FFKM, which have a maximum operating temperature of about 300 °C, or mica gaskets, exhibiting temperature resistance up to approximately 1000 °C. However, it is noteworthy that mica materials may necessitate a substantial compression force, which might be difficult to achieve considering the cyclic operation of the gate. In the event of elastomers being selected, the design has to be adapted to reduce the maximum gate temperature, and this can, for example, be achieved by incorporating insulation in the upper section where it interfaces with the reduction reactor.

Finally, the prototype's steel shell maximum temperature is located at the lower internal corner of the reduction reactor (where the insulation is thinner) and increases from 61.6 °C at the start of the simulation to 209 °C at the end of the fifth cycle. On the other hand, the minimum steel shell's temperature is located in the upper external corner of the reduction reactor and increases from 35.7 °C to 37.4 °C. A maximum temperature of approximately 210 °C for the steel shell is acceptable for this material's operation and is on a par with the reported cavity receiver–reactor's experimental results [22]. Nevertheless, it is not recommended to operate with such high temperatures at the reactor surface, as they will lead to an increased heat loss to the ambient. In the model, the minimum temperatures might pose a challenge to the operation as they will cause condensation inside the oxidation reactor. Consequently, an external insulation jacket for the steel shell will be considered in future development stages to reduce heat losses to ambient.

4.2 Component Sizing. Aiming at supporting the design development of the prototype test stand, the heating unit in the reduction reactor was sized. It is estimated that for the analyzed design, the heating unit will require at least a 1450 W capacity. For this assessment, initially, a power–time curve, for the heating element during each reduction step, was obtained by utilizing a temperature probe on the component's body in ANSYS MECHANICAL. The curve was integrated and then averaged for the duration of the reduction step to assess the average energy required to provide the same total energy to the heating element as in the simulated case. An average for the five reduction steps was calculated. Hence, the heating unit is reasonably dimensioned.

To model the initial heat up of the test stand utilizing the sized heating element, an additional transient heat transfer simulation was run. Results show that after 5 h of heating the test stand, the redox material could be reduced within 8 min and achieve a temperature of about 1450 °C.

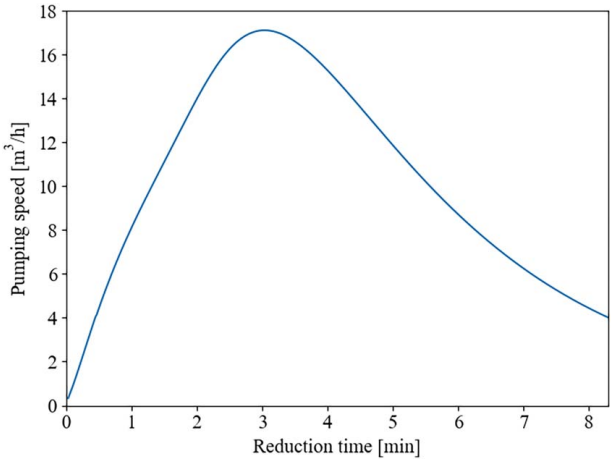

Fig. 6 Pumping speed required to maintain a target pressure of 1 mbar during the fifth cycle of the base case. Base case operational parameters are given in Table 3.

In this study, we assume that vacuum pump used for operation during reduction has a pumping speed that can be controlled and will be capable of constantly removing the oxygen released by the redox material to maintain a target pressure of 1 mbar. The pumping speed required to achieve this type of operation during one reduction step is portrayed in Fig. 6. The estimation considers the fifth cycle, where δ_{red} achieves its maximum value and assumes $\delta_{ox} = 0$, in order to obtain a large oxygen quantity and therefore a conservative pumping speed. A maximum required pumping speed of 17 m^3/h is predicted, for which two-stage rotary vane pump seems appropriate. A commercially available two-stage rotary vane pump with a pumping speed of 18 m^3/h would be suitable for application in the R2Mx prototype test stand. With such a vacuum pump, initial pumping, when the entire test stand is brought into vacuum from atmospheric pressure, would require less than 1 min, considering the entire test stand volume and 10% open porosity for the insulation.

4.3 Operational Parameters Evaluation. The measure used in this study to determine a reasonable duration of the reduction steps and to assess the energy losses of each cycle is the energy conversion ratio. In Fig. 7(*a*), the energy conversion ratio for each cycle is illustrated. Each of the reduction reactions is stopped once the maximum energy conversion ratio (depicted by a black dot in Fig. 7(*a*)) is reached. In the base case, energy conversion ratio increases after each cycle. The maximum energy conversion ratio of the first cycle is 0.0416, while for the third and fifth cycle is 0.0438 and 0.0445, respectively. The duration of each reduction step varies accordingly from 8.6 min in the first cycle to 8.3 min in the third cycle and 8.3 min in the fifth cycle. These are rough estimates, considering a time discretization size of 20 s.

Acknowledging that the maximum achieved energy conversion ratio determines the length of the reduction step and its dependency on the reduction oxygen partial pressure, an analysis involving the reduction step duration and oxygen partial pressure was performed. Figure 7(*b*) illustrates the relationship between energy conversion ratio of the second reduction step and the partial pressure of oxygen, with the duration of the reduction step portrayed by a black dot. Reducing the oxygen partial pressure from 1 mbar by a factor of ten to 0.1 mbar increased the energy conversion ratio by 60% to 0.0668. However, when the oxygen partial pressure was increased from 1 mbar to 10 mbar, the energy conversion ratio decreased to 0.0260 (37.5% decrease). Despite these changes in energy conversion ratio, the length of the reduction step is almost

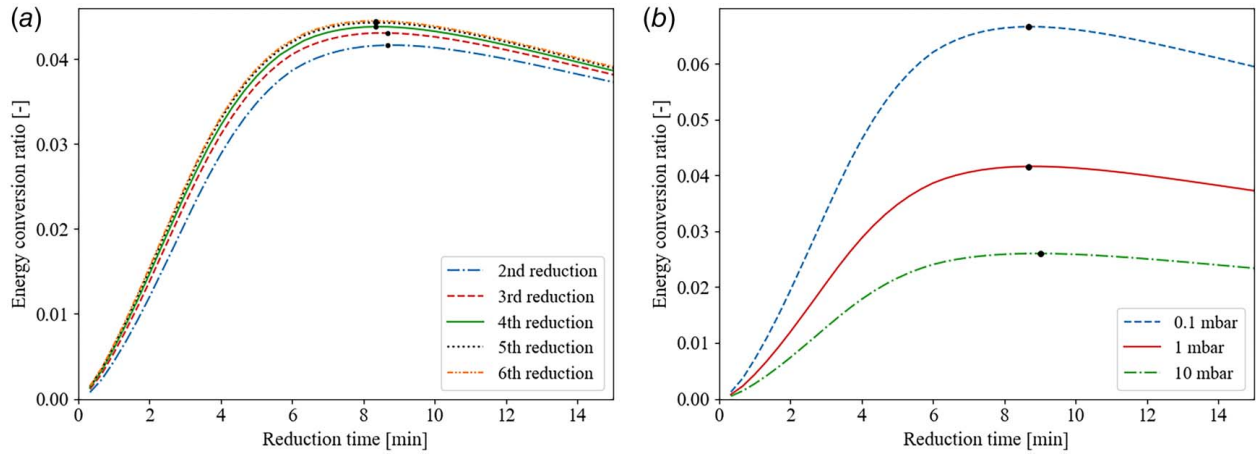

Fig. 7 (*a*) Energy conversion ratio versus time of the reduction step and (*b*) energy conversion ratio of first cycle versus time of the reduction step, for different oxygen partial pressures. The maximum energy conversion ratio in each reduction step is marked by a black dot, and at this point, the reduction reaction was stopped and RMA moved to the oxidation reactor. Base case operational parameters are given in Table 3.

equal at 8.6 min for 1 mbar and 0.01 mbar, and 9 min for 10 mbar. In a receiver–reactor setting, a low oxygen partial pressure can be achieved by means of sweep gas utilization or vacuum pumping, and in this case, we focus on vacuum pumping since it leads to higher cycle efficiencies [44]. Literature reports that generally the pumping efficiency at 1 mbar is approximately 10% and drops below 3% at 0.1 mbar [24]. This is due to thermal losses, which increase with the compression ratio, and leakage, which increases with the decreasing pressure. Generally, vacuum-pumped solar reactors operate at an optimum efficient pressure between 0.1 and 10 mbar. Based on the model results, which include effects on heat transfer due to the effective heat capacity, but omitting actual mass transfer, we can expect that at these pressures ranges, the duration of the reduction step remains rather constant.

4.4 Parametric Analysis. A parametric analysis has been performed to evaluate different modes of operation of the oxidation reactor. For this, three scenarios were developed and compared to the base case. The first scenario named "6 min" has the same operating conditions as the base case with the exception of the duration of the oxidation reaction, which in this case has a length of 6 min. The second scenario "10 min" similarly as before shares the same operating parameters as the base case, but has a longer oxidation reaction of 10 min. Finally, the scenario "No cooling" has the same operating parameters as the base case (8-min-long oxidation), but no cooling of the RPC before oxidation is considered. This scenario would require a large excess of oxidizer to achieve significant oxidation of the redox material, but nevertheless it represents a possible operation approach of the prototype. For the parametric analysis, only three consecutive cycles for each scenario were simulated.

Figure 8(*a*) shows the average temperature of the ceria RPC throughout the third cycle in each scenario and the base case. The minimum average temperature of the redox material is obtained after the oxidation reaction, in all scenarios. In the "6 min" scenario, the ceria RPC reaches a minimum average temperature of 794.6 °C, a 6% temperature increase from the base case. The minimum average temperature for the ceria RPC in the "10 min" scenario is 701.1 °C, which corresponds to an 11% decrease from the base case's minimum average temperature. On the other hand, the "No cooling" scenario has the highest minimum RPC average

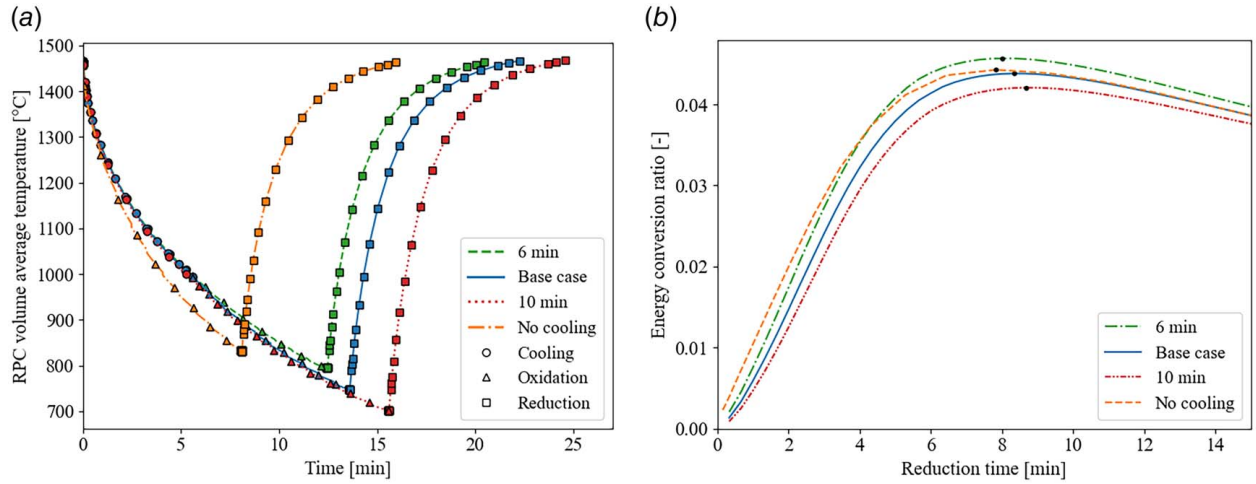

Fig. 8 (*a*) RPC volume average temperature for the duration of the entire third cycle, for each scenario. The markers do not represent all the data points used, but rather aid the distinction between the process steps. (*b*) Energy conversion ratio of the third cycle of each of the investigated scenarios. The black dot denotes the moment at which the maximum energy conversion ratio is achieved and the reduction reaction stopped. Base case operational parameters are given in Table 3.

temperature of 832.9 °C at a 4% increase from the base case. The "No cooling" scenario achieves the highest ceria RPC temperature since the redox material has no additional cooling period, as it is directly cooled in the steam atmosphere as it undergoes oxidation. By comparison to cooling solely under the steam atmosphere during oxidation, cooling through radiation in the oxidation reactor and then in the steam atmosphere leads to a lower cooling rate as portrayed in Fig. 8(*a*). In all scenarios, the minimum average ceria RPC temperature increased with a larger number of performed cycles. Average temperatures for the redox material after reduction in the third cycle were found to be 1463 °C, 1467.2 °C, and 1462 °C for the scenarios "6 min," "10 min," and "No cooling," respectively.

Figure 8(*b*) illustrates the highest achieved energy conversion ratio and length of reduction for each of the scenarios. The energy conversion ratio in each of the examined scenarios increases as the number of cycles also increases, as seen in the base case. The "No cooling" scenario has the shortest reduction step of 7.8 min followed by the "6 min" scenario at 8 min (2% more). For the "10 min" scenario, the reduction step length is 8.6 min, showing a 3.8% increase in duration than the base case. It is interesting to note that for all scenarios, the durations of the reduction step are fairly constant, even though the oxidation procedure and duration are altered significantly, showing the limited effect of the oxidation step on reduction times for the investigated cases.

5 Summary and Conclusions

A transient heat transfer model of a prototype test stand design for a R2Mx type reactor has been developed and used. With the model of the prototype test stand design, five consecutive pressure and temperature swing thermochemical cycles to split water are simulated. Each cycle includes a reduction step, redox material transport between reaction zones, and an oxidation step.

Design choices, such as material selection, were evaluated considering temperature profiles for each component. For all of the simulated reactor parts, the initial material selection was adequate, posing no risk to operation. In fact, the insulation of the oxidation chamber can be replaced by a material with lower classification temperature, to achieve a less conservative design. Furthermore, findings confirmed that as the number of cycles advance the redox material's average temperature after oxidation increases. The converged ceria RPC's average temperature after oxidation is estimated to be approximately 760 °C and is reached after ten cycles in the base case scenario. Throughout the cycles, the transport step has only a very minor impact on the redox material cooling. In addition, for the initial prototype design, the heating unit in the reduction reactor has been sized to about 1450 W and the maximum vacuum pump's pumping speed to 17 m^3/h. Further results indicate that changes in oxygen partial pressure during reduction do not affect the duration of the reduction step in the R2Mx prototype test stand, but will affect the vacuum pumping speed demand (assuming that the reduction reaction is not limited by kinetics and nor is the mass transfer limit defined by the vacuum pump).

A parametric analysis has been performed to evaluate different modes of operation of the oxidation reactor. With this, we found evidence suggesting that the procedure and length of the oxidation only have a limited effect on the duration of the reduction in the evaluated step durations and setup. Approximate reaction durations for reasonable operation of the prototype design include reduction times of 8–10 min and oxidations in the range of 6–10 min. The results obtained in this study guide the initial development of an R2Mx reactor-type prototype.

Acknowledgment

The project on which this report is based was funded by the German Federal Ministry for Economics and Climate Action under the funding code Redox3D (03EE5124A). The authors are responsible for the content of this publication.

Conflict of Interest

There are no conflicts of interest.

Data Availability Statement

The datasets generated and supporting the findings of this article are obtainable from the corresponding author upon reasonable request.

Nomenclature

h = convective film coefficient, W/K m^2
p = pressure, Pa
t = time, s
A = area, m^2
T = temperature, °C
$c_{p,(.)}$ = specific heat capacity, J/kg K
$c_{p,\mathrm{eff}}$ = modified heat capacity, J/kg K
$k_{(.)}$ = thermal conductivity, W/m K
k_{eff} = effective thermal conductivity, W/m K
$\dot{n}_{\mathrm{fuel}}$ = rate of change of amount of fuel, mol/s
$n_{(.)}$ = amount of substance, mol
p_{O_2} = oxygen partial pressure, Pa
p_{H_2} = hydrogen partial pressure, Pa
p_{H_2O} = steam partial pressure, Pa
p_0H_2O = reference pressure, Pa
r_{econv} = energy conversion ratio
F_{ij} = view factor from surface i to surface j
K_{eq} = equilibrium reaction constant
$M_{\mathrm{CeO_2}}$ = molar mass of ceria, kg/mol
$\dot{Q}_{\mathrm{aux}}$ = rate of parasitic energy consumption, W
$\dot{Q}_{\mathrm{solar}}$ = rate solar irradiative energy input, W
X_{ox} = conversion of H_2O to H_2
ΔH_{O} = reaction enthalpy, kJ/mol
$\Delta_R G$ = free Gibbs energy of reaction, kJ
HHV = higher heating value, kJ/mol

Greek Symbols

β = extinction coefficient, 1/m
δ = deviation from stoichiometry
$\varepsilon_{(.)}$ = emissivity
η_{sf} = solar to fuel efficiency
$\rho_{(.)}$ = density, kg/m^3
σ = Stefan–Boltzmann constant, W/m^2 K^4
Φ_{dual} = dual-scale porosity

Subscripts

amb = ambient
CeO_2 = ceria
ins = insulation
ox = oxidation
s = surface
ss = stainless steel
st = steam
red = reduction

Abbreviations

CFD = computational fluid dynamics
FEA = finite element analysis
ppi = pores per inch
RMA = redox material assembly
RPC = reticulated porous ceramic
TES = thermal energy storage

References

[1] Fuel Cells and Hydrogen 2 Joint Undertaking, 2019, "Hydrogen Roadmap Europe: A sustainable pathway for the European Energy Transition," Report, EU Publications Office, Luxembourg," https://data.europa.eu/doi/10.2843/341510, Accessed July 29, 2024

[2] La Calle, A., and Bayon, A., 2019, "Annual Performance of a Thermochemical Solar Syngas Production Plant Based on Non-Stoichiometric CeO_2," Int. J. Hydrogen Energy, **44**(3), pp. 1409–1424.

[3] Panlener, R. J., Blumenthal, R. N., and Garnier, J. E., 1975, "A Thermodynamic Study of Nonstoichiometric Cerium Dioxide," J. Phys. Chem. Solids, **36**(11), pp. 1213–1222.

[4] Mogensen, M., Sammes, N. M., and Tompsett, G. A., 2000, "Physical, Chemical and Electrochemical Properties of Pure and Doped Ceria," Solid State Ionics, **129**(1), pp. 63–94.

[5] Koepf, E., Zoller, S., Luque, S., Thelen, M., Brendelberger, S., González-Aguilar, J., Romero, M., and Steinfeld, A., 2018, "Liquid Fuels From Concentrated Sunlight: An Overview on Development and Integration of a 50 kW Solar Thermochemical Reactor and High Concentration Solar Field for the SUN-to-LIQUID Project," SolarPACES, Casablanca, Morocco, Oct. 2–5, American Institute of Physics, p. 180012.

[6] Ermanoski, I., Siegel, N. P., and Stechel, E. B., 2013, "A New Reactor Concept for Efficient Solar-Thermochemical Fuel Production," ASME J. Sol. Energy Eng., **135**(3), p. 031002.

[7] Abanades, S., and Flamant, G., 2006, "Thermochemical Hydrogen Production From a Two-Step Solar-Driven Water-Splitting Cycle Based on Cerium Oxides," Sol. Energy, **80**(12), pp. 1611–1623.

[8] Lidor, A., Fend, T., Roeb, M., and Sattler, C., 2021, "High Performance Solar Receiver–Reactor for Hydrogen Generation," Renewable Energy, **179**(16), pp. 1217–1232.

[9] Thanda, V. K., Fend, T., Laaber, D., Lidor, A., von Storch, H., Säck, J. P., Hertel, J., et al.et al., 2022, "Experimental Investigation of the Applicability of a 250 kW Ceria Receiver/Reactor for Solar Thermochemical Hydrogen Generation," Renewable Energy, **198**(18), pp. 389–398.

[10] Welte, M., Barhoumi, R., Zbinden, A., Scheffe, J. R., and Steinfeld, A., 2016, "Experimental Demonstration of the Thermochemical Reduction of Ceria in a Solar Aerosol Reactor," Ind. Eng. Chem. Res., **55**(40), pp. 10618–10625.

[11] Brendelberger, S., and Sattler, C., 2015, "Concept Analysis of an Indirect Particle-Based Redox Process for Solar-Driven H_2O/CO_2 Splitting," Sol. Energy, **113**(3), pp. 158–170.

[12] Brendelberger, S., Holzemer-Zerhusen, P., Vega Puga, E., Roeb, M., and Sattler, C., 2022, "Study of a New Receiver-Reactor Cavity System With Multiple Mobile Redox Units for Solar Thermochemical Water Splitting," Sol. Energy, **235**(5), pp. 118–128.

[13] Diver, R. B., Miller, J. E., Allendorf, M. D., Siegel, N. P., and Hogan, R. E., 2008, "Solar Thermochemical Water-Splitting Ferrite-Cycle Heat Engines," ASME J. Sol. Energy Eng., **130**(4), p. 041001.

[14] Diver, R. B., Miller, J. E., Siegel, N. P., and Moss, T. A., 2010, "Testing of a CR5 Solar Thermochemical Heat Engine Prototype," ASME International Conference on Energy Sustainability, Phoenix, AZ, May 17–22, p. 2.

[15] Patankar, A. S., Wu, X., Chao, W., Tuller, H. L., and Ghoniem, A., 2022, "A Reactor Train System for Efficient Solar Thermochemical Fuel Production," ASME J. Sol. Energy Eng., **144**(6), p. 061014.

[16] Weber, A., Grobbel, J., Neises-von Puttkamer, M., and Sattler, C., 2023, "Swept Open Moving Particle Reactor Including Heat Recovery for Solar Thermochemical Fuel Production," Sol. Energy, **266**(18), pp. 112–178.

[17] Ermanoski, I., Grobbel, J., Singh, A., Lapp, J., Brendelberger, S., Roeb, M., Sattler, C., Whaley, J., McDaniel, A., and Siegel, N. P., 2016, "Design and Construction of a Cascading Pressure Reactor Prototype for Solar-Thermochemical Hydrogen Production," AIP Conference Proceedings, SolarPACES, Cape Town, South Africa, Oct. 13–16, p. 1734.

[18] Bulfin, B., Miranda, M., and Steinfeld, A., 2021, "Performance Indicators for Benchmarking Solar Thermochemical Fuel Processes and Reactors," Front. Energy Res., **9**, p. 677980.

[19] Kaneko, H., Ishikawa, Y., Lee, C., Hart, G., Stein, W., and Tamaura, Y., 2011, "Simulation Study of Tokyo Tech Rotary-Type Solar Reactor on Solar Field Test at CSIRO in Australia," ASME International Conference on Energy Sustainability, Washington, DC, Aug. 7–10, pp. 1673–1680.

[20] Lapp, J., Davidson, J. H., and Lipiński, W., 2013, "Heat Transfer Analysis of a Solid-Solid Heat Recuperation System for Solar-Driven Nonstoichiometric Redox Cycles," ASME J. Sol. Energy Eng., **135**(3), p. 031004.

[21] Zoller, S., Koepf, E., Nizamian, D., Stephan, M., Patané, A., Haueter, P., Romero, M., et al., 2022, "A Solar Tower Fuel Plant for the Thermochemical Production of Kerosene From H_2O and CO_2," Joule, **6**(7), pp. 1606–1616.

[22] Zoller, S., Koepf, E., Roos, P., and Steinfeld, A., 2019, "Heat Transfer Model of a 50 kW Solar Receiver–Reactor for Thermochemical Redox Cycling Using Cerium Dioxide," ASME J. Sol. Energy Eng., **141**(2), p. 021014.

[23] Säck, J.-P., Breuer, S., Cotelli, P., Houaijia, A., Lange, M., Wullenkord, M., Spenke, C., Roeb, M., and Sattler, C., 2016, "High Temperature Hydrogen Production: Design of a 750 KW Demonstration Plant for a Two Step Thermochemical Cycle," Sol. Energy, **135**(13), pp. 232–241.

[24] Brendelberger, S., Rosenstiel, A., Lopez-Roman, A., Prieto, C., and Sattler, C., 2020, "Performance Analysis of Operational Strategies for Monolithic Receiver-Reactor Arrays in Solar Thermochemical Hydrogen Production Plants," Int. J. Hydrogen Energy, **45**(49), pp. 26104–26116.

[25] Lidor, A., Aschwanden, Y., Häseli, J., Reckinger, P., Haueter, P., and Steinfeld, A., 2023, "High-Temperature Heat Recovery From a Solar Reactor for the Thermochemical Redox Splitting of H_2O and CO_2," Appl. Energy, **329**(1), p. 120211.

[26] Marxer, D., Furler, P., Takacs, M., and Steinfeld, A., 2017, "Solar Thermochemical Splitting of CO_2 Into Separate Streams of CO and O_2 With High Selectivity, Stability, Conversion, and Efficiency," Energy Environ. Sci., **10**(5), pp. 1142–1149.

[27] Li, S., Wheeler, V. M., Kreider, P. B., Bader, R., and Lipiński, W., 2018, "Thermodynamic Analyses of Fuel Production via Solar-Driven Non-Stoichiometric Metal Oxide Redox Cycling. Part 2. Impact of Solid–Gas Flow Configurations and Active Material Composition on System-Level Efficiency," Energy Fuels, **32**(10), pp. 10848–10863.

[28] Miller, J. E., McDaniel, A. H., and Allendorf, M. D., 2014, "Considerations in the Design of Materials for Solar-Driven Fuel Production Using Metal-Oxide Thermochemical Cycles," Adv. Energy Mater., **4**(2), p. 1300469.

[29] Falter, C. P., Sizmann, A., and Pitz-Paal, R., 2015, "Modular Reactor Model for the Solar Thermochemical Production of Syngas Incorporating Counter-Flow Solid Heat Exchange," Sol. Energy, **122**(12), pp. 1296–1308.

[30] Siegrist, S., von Storch, H., Roeb, M., and Sattler, C., 2019, "Moving Brick Receiver–Reactor: A Solar Thermochemical Reactor and Process Design With a Solid–Solid Heat Exchanger and On-Demand Production of Hydrogen and/or Carbon Monoxide," ASME J. Sol. Energy Eng., **141**(2), p. 021009.

[31] Rath, A. G., 2017, "Altraform KVR 164-502," Data Sheet, p. 5, https://www.rath-group.com/fileadmin/content/Rath-Group/Downloads/Broschueren_Produkte/RATH_VacuumFormedShapes_201710_DE.pdf, Accessed July 29, 2024

[32] Schäppi, R., Rutz, D., Dähler, F., Muroyama, A., Haueter, P., Lilliestam, J., Patt, A., Furler, P., and Steinfeld, A., 2022, "Drop-In Fuels From Sunlight and Air," Nature, **601**(7891), pp. 63–68.

[33] Furler, P., and Steinfeld, A., 2015, "Heat Transfer and Fluid Flow Analysis of a 4 kW Solar Thermochemical Reactor for Ceria Redox Cycling," Chem. Eng. Sci., **137**(18), pp. 373–383.

[34] Ackermann, S., Takacs, M., Scheffe, J., and Steinfeld, A., 2017, "Reticulated Porous Ceria Undergoing Thermochemical Reduction With High-Flux Irradiation," Int. J. Heat Mass Transfer, **107**(4), pp. 439–449.

[35] Grobbel, J., 2019, "Modeling Solar Particle Receivers With the Discrete Element Method," Ph.D. thesis, RWTH Aachen University, DLR, Aachen, NRW, Germany.

[36] Holzemer-Zerhusen, P., Brendelberger, S., Roeb, M., and Sattler, C., 2021, "Oxygen Crossover in Solid–Solid Heat Exchangers for Solar Water and Carbon Dioxide Splitting: A Thermodynamic Analysis," ASME J. Energy Resour. Technol., **143**(7), p. 071301.

[37] Arifin, D., and Weimer, A. W., 2018, "Kinetics and Mechanism of Solar-Thermochemical H_2 and CO Production by Oxidation of Reduced CeO_2," Sol. Energy, **160**(2), pp. 178–185.

[38] Bale, C. W., Bélisle, E., Chartrand, P., Decterov, S. A., Eriksson, G., Gheribi, A. E., Hack, K., et al., 2016, "FactSage Thermochemical Software and Databases, 2010–2016," Calphad, **54**, pp. 35–53.

[39] Touloukian, Y. S., and DeWitt, D. P., 1972, "Thermophysical Properties of Matter—The TPRC Data Series. Volume 8. Thermal Radiative Properties—Nonmetallic solids. (Reannouncement)," Data Book, United States, https://www.osti.gov/biblio/5447756, Accessed July 29, 2024

[40] Ansys® Academic Research Mechanical Release 18.0, "Computer Software Material Library," ansys-granta-materials-data-brochure.pdf, Accessed July 29, 2024

[41] Modest, M., 2013, *Radiative Heat Transfer*, Academic Press, Oxford, UK.

[42] ASME Research and Technology Committee on Water and Steam in Thermal Systems, Subcommittee on Properties of Steam, 2000, *ASME International Steam Tables for Industrial Use Based on the IAPWS Industrial Formulation 1997 for the Thermodynamic Properties of Water and Steam (IAPWS-IF97)*, American Society of Mechanical Engineers, New York.

[43] Weber, A., 2021, "Simulation of a New Receiver Reactor Concept," M.Ed. thesis, University Koblenz-Landau, Koblenz, NRW, Germany.

[44] Bulfin, B., Call, F., Lange, M., Lübben, O., Sattler, C., Pitz-Paal, R., and Shvets, I. V., 2015, "Thermodynamics of CeO_2 Thermochemical Fuel Production," Energy Fuels, **29**(2), pp. 1001–1009.